

# FIPER: Generalizable Factorized Features for Robust Low-Level Vision Models

Yang-Che Sun<sup>1</sup> Cheng Yu Yeo<sup>1</sup> Ernie Chu<sup>2</sup> Jun-Cheng Chen<sup>3</sup> Yu-Lun Liu<sup>1</sup>

<sup>1</sup>National Yang Ming Chiao Tung University <sup>2</sup>Johns Hopkins University <sup>3</sup>Academia Sinica

## Abstract

In this work, we propose using a unified representation, termed **Factorized Features**, for low-level vision tasks, where we test on **Single Image Super-Resolution (SISR)** and **Image Compression**. Motivated by the shared principles between these tasks, they require recovering and preserving fine image details—whether by enhancing resolution for SISR or reconstructing compressed data for Image Compression. Unlike previous methods that mainly focus on network architecture, our proposed approach utilizes a basis-coefficient decomposition as well as an explicit formulation of frequencies to capture structural components and multi-scale visual features in images, which addresses the core challenges of both tasks. We replace the representation of prior models from simple feature maps with Factorized Features to validate the potential for broad generalizability. In addition, we further optimize the pipelines by leveraging the mergeable-basis property of our Factorized Features, which consolidates shared structures on multi-frame compression and super-resolution. Extensive experiments show that our unified representation delivers state-of-the-art performance, achieving an average relative improvement of 204.4% in PSNR over the baseline in Super-Resolution (SR) and 9.35% BD-rate reduction in Image Compression compared to the previous SOTA. Please see our project page at [jayisaking.github.io/FIPER](https://jayisaking.github.io/FIPER).

## 1. Introduction

Single Image Super-Resolution (SISR) aims to reconstruct high-quality images from low-resolution counterparts. Specifically, the key lies in accurately restoring fine details and reconstructing the correct arrangement of visual features. Thus, geometric correspondences or repetitive patterns, such as stripes, grids, or textures, are commonly used for evaluation due to their rich details that are crucial to image fidelity. Early CNN-based approaches [23, 52] laid the foundation for SISR, which was later enhanced with GAN-based methods [40] for improved perceptual realism. Follow-up Transformer-based networks [14] address non-local dependencies, with subsequent Swin Transformer-

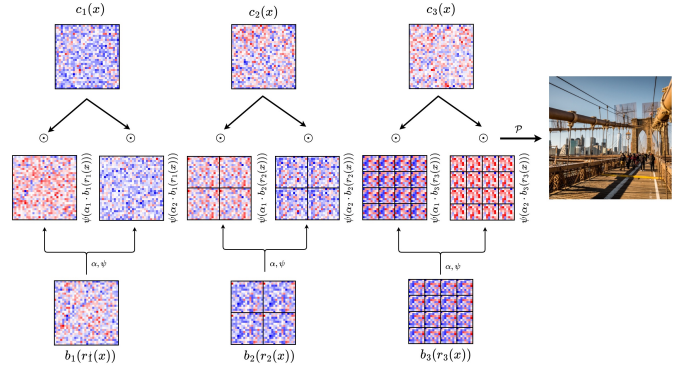


Figure 1. **The Proposed Factorized Features.** With explicit formulation of repetitive patterns and high frequency components, images can be represented with fine-grained details, which is especially useful for low-level vision tasks such as Super-Resolution and Image Compression. Note that in this figure  $\alpha = \{1, 16\}$  and  $\psi = \sin(\cdot)$ .

based approaches sparking tremendous advancements [17, 18, 21], which then inspire more and more complex, delicate designs of heavy network architectures in SISR. However, these prior works have primarily focused on network architecture design rather than addressing the capability of representation. The visual patterns and the inherent nature of image content structure that play an influential role in SISR have not been explicitly considered in the representation learning process. This raises a critical question: beyond a simple network output, can we derive a formulation that more effectively captures these patterns and aligns with the goals of SISR? On the other hand, image compression serves as a fundamental task in low-level vision applications, where the traditional compression standards [35, 79, 82] lay the groundwork. The emerging learned image compression models [3, 8, 19, 30, 55, 67], compression algorithms of which mostly follow the pixel-space transform coding [8, 28] paradigm, then introduce a variety of networks [55, 83] or difference losses [31] to further optimize compression efficiency by learning more compact latent representations and improving reconstruction quality. Specifically, they convert pixels into compact repre-

sentations through a transform module, which eliminates the redundancy and reduces the bit cost in the subsequent entropy coding process. However, the core challenge of image compression is to accurately reconstruct the information lost during compression and quantization. In other words, the models are to recover the impaired components in images, which can essentially be viewed as reconstructing a high-quality image from its ‘low-resolution’ version, much like Super-Resolution or all other common low-level vision tasks such as image restoration, deblurring, denoising, etc.

Based on the aforementioned analysis, it becomes clear that although these tasks appear to be distinct, they share mutual similarities in two key aspects: (1) The tasks require models to restore fine details from low-quality image content, as well as implicitly capture and reconstruct repetitive structural elements. (2) They aim to conserve image quality, either by enhancing resolution or efficiently compressing data without significant loss of perceptual fidelity. Hence, inspired by recent advances in decomposition fields and matrices factorization in 3D scene modeling [7, 9, 11, 12, 26, 27, 68], we propose a unified representation, **Factorized Features**, with generalizable Coefficient Backbone and Basis Transformer for learned coefficient and basis, respectively. This approach explicitly captures multi-scale visual features and repetitive structural components in images through a basis-coefficient decomposition. The resulting representation strikes a balance between being compact and information-rich, enabling the resolution of structural ambiguities and the precise modeling of image details through a multi-frequency formulation.

Finally, we propose merging the bases for multi-image processing by consolidating multiple bases into one through a network, as in traditional Discrete Fourier Transform, all signals of same size are reconstruct by the same set of basis functions, and we argue that learned shared basis can leverage the mutual information across multiple images to capture common structures.

The main contributions of this paper are summarized as follows:

- We identify the weakness of previous similar representations and propose a refined representation, Factorized Features, based on thorough analysis as in Sec. 3.1 for coarse and fine details of images via explicitly modeling multi-scale visual features and structural components.
- We generalize such image descriptor to learned settings on super-resolution and image compression, with potential applicability to broader low-level vision tasks.
- We demonstrate state-of-the-art performance on benchmarks for both super-resolution and image compression through extensive experiments.

## 2. Related Works

**Super-Resolution (SR).** Image super-resolution (SISR) aims to reconstruct high-resolution (HR) images from low-resolution (LR) inputs, which is crucial for computer vision. Early CNN-based methods [23, 36, 52, 76, 95] introduced residual [20, 41, 51, 54, 81, 93, 94] and recursive learning [18, 77]. GAN-based approaches [40, 41, 84, 85] improved perceptual quality but faced spatial locality constraints, leading to Transformer-based SISR models [14, 46]. SwinIR [48] integrated window attention with Swin Transformer [58], inspiring further advancements [20, 21, 91, 96]. Hybrid models like CRAFT [43], DAT [17], and HAT [15] optimize feature aggregation, while RGT [18] enhances spatial details efficiently.

**Image Compression (IC).** Deep learning surpasses traditional compression methods like JPEG [82] and JPEG-2000 [79], with CNN-based [4, 8, 29], Transformer-based [24, 38, 86, 97], and GAN-based [25, 61, 62, 73] approaches improving performance. ELIC [32] introduced adaptive coding, LIC TCM [55] combined CNNs and Transformers, and eContextformer [39] leveraged spatial-channel attention. GroupedMixer [44] introduced token mixers, while Wavelet Conditional Diffusion [75] balanced perceptual quality and distortion.

Our work diverges from these trends by introducing Factorized Features, a unified framework modeling both visual and structural features to enhance performance across super-resolution and image compression.

## 3. Methods

In this section, we start by revisiting several previous renowned representations for images, e.g., 2D Fourier Transform, Learnable Fourier Series [57], and Factor Fields [12], and delve into the motivation and how we resolve the weaknesses of these formulations by our Factorized Features in Sec. 3.1. Next, we discuss how to integrate such strategy into learned settings of Super-Resolution in Sec. 3.2 and Image Compression Sec. 3.3. Note that the background of learned image compression is provided in supplementary materials.

### 3.1. Formulation of Factorized Features

Fourier Transform has been long used in many scenarios to represent periodic or finite signals with a group of sinusoidal functions. In practice, it often takes the form of Discrete Cosine Transform for real-valued 2D discrete signal  $f$  with height  $H$  and width  $W$ :

$$f[x, y] = \sum_{u=0}^{H-1} \sum_{v=0}^{W-1} S_{u,v} \cos \left[ \frac{\pi u}{H} \left( x + \frac{1}{2} \right) \right] \cos \left[ \frac{\pi v}{W} \left( y + \frac{1}{2} \right) \right] \quad (1)$$

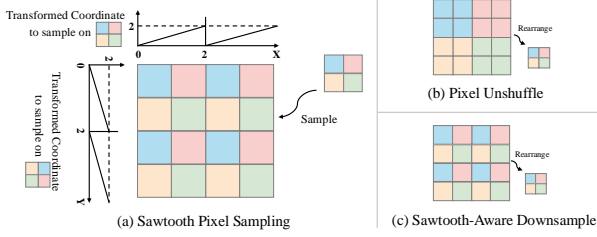


Figure 2. **The correlation between coordinate transformation and downsampling.** (a) The sawtooth transformation example with  $k = 2$ . (b) The PixelUnShuffle downsample. (c) To explicitly model the information for sampling with a sawtooth, we rearrange the feature map in a dilation-like manner in the downsample layer of the Basis Swin Transformer. This way, the feature sampled would capture the information in the original layout correctly; in other words,  $I = \text{Sawtooth-Pixel-Sampling}(\text{Sawtooth-Aware-Downsample}(I))$

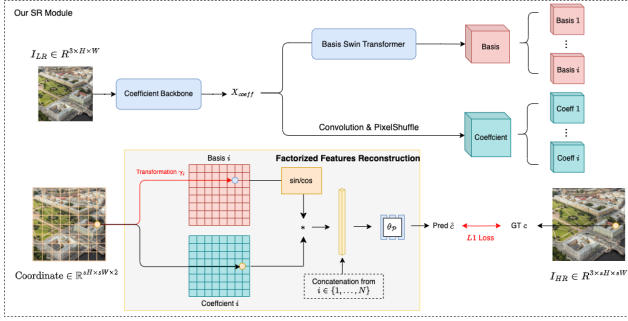


Figure 3. **The overall pipeline of image super-resolution with our Factorized Features.** Given a low-resolution image  $I_{LR}$ , we first extract the coefficient feature map  $X_{\text{coeff}}$  with the coefficient backbone, which is then decoded into coefficients and passed through the basis Swin Transformer for basis, separately. Finally, as in Eq. (8), the coefficient and basis are sampled, multiplied, and decoded for final high-resolution output  $I_{HR}$ , where  $s$ ,  $H$ , and  $W$  denote the scale factor, height, and width, respectively.

where  $S_{u,v}$  is the amplitude.

Without the loss of generality, we consider square images in this work, with edge length (and also the period) denoted as  $T$ :

$$f[x, y] = \sum_{u=0}^{T-1} \sum_{v=0}^{T-1} S_{u,v} \cos \left[ \frac{2\pi}{T} (ux + vy) - \xi_{u,v} \right] \quad (2)$$

where  $x < T$ ,  $y < T$ , and  $\xi_{u,v}$  is phase shift. In image processing tasks, the goal is to learn  $S$  and  $\xi$ , then use the formula above to reconstruct high-quality images from degraded inputs. To achieve this, [57] treats  $S$  and  $\xi$  as learnable parameters, allowing the model to optimize them for better reconstruction. Furthermore, the frequencies  $u$  and  $v$  are also designed to be promptable by the model, enabling dynamic adaptation to spatial-varying high- and low-frequency components.

More generally, we can formulate it as the multiplication of coefficient  $c$  and basis  $b$  with simplified notation, and in this work, we use  $\mathbf{x}$  to represent the pixel coordinates  $(x, y)$ :

$$f(\mathbf{x}) = \sum_{i=1}^N c_i \cdot b_i(\mathbf{x}), \quad (3)$$

where  $b_i(\mathbf{x}) = \cos[(u_i x + v_i y) - \xi_i]$  and  $N$  denotes the number of frequency components.

**Spatially Variant Coefficient.** Intuitively, the local frequency spectrum of a signal is spatially variant, meaning that different regions exhibit distinct spectral characteristics, e.g., certain regions of an image do not require high-frequency components. Therefore, in this work, we argue that coefficient  $c_i$  should be spatial-varying, which is different from previous works, i.e.,

$$f(\mathbf{x}) = \sum_{i=1}^N c_i(\mathbf{x}) \cdot b_i(\mathbf{x}). \quad (4)$$

**Learned Non-uniform Basis.** Previous works learn basis through frequencies  $u, v$  and phase shift  $\xi$  [42, 47, 57]; however, constructing signals with definitive sets of uniform sinusoidal harmonic functions does not facilitate the utmost details; in other words, since low-frequency components typically require more energy [45], during the learning process with training losses of MAE or MSE, models would attend more to low-frequency parts and sacrifice local details, and the predefined nature of these sinusoidal functions further restricts local flexibility, making fine-grained adjustments more challenging. As shown in Fig. 5, higher frequency components converge slower than their counterpart. Hence, in this work, we generate the entire basis map  $b_i \in R^{T \times T}$  for better fitting and local reconstruction.

To this end, we have introduced our rough idea: Under the generalizable setting, we use networks to generate a multi-channel coefficient map and a multi-channel basis map and combine them together. In this work, the composition process happens in the end with a projection function  $\mathcal{P}$  to form RGB images  $\hat{I}$ :

$$\hat{I}(\mathbf{x}) = \mathcal{P} \left( \text{Concat}_{i=1}^N \left\{ c_i(\mathbf{x}) \cdot b_i(\mathbf{x}) \right\} \right). \quad (5)$$

In contrast to previous works which employ fourier bottlenecks [57], or frequency decomposition blocks [42, 45, 47] among model blocks, here we seek to address a fundamental question: Can a well-learned representation effectively replace the simple feature map output? That is, our solution is meant to be applied directly on networks to represent **any** images.

**Coordinate Transformation.** The success of Fourier-based representation originates from its sinusoidal decomposition. By using such periodic functions, one can effectively analyze and reconstruct signals with the enforcement

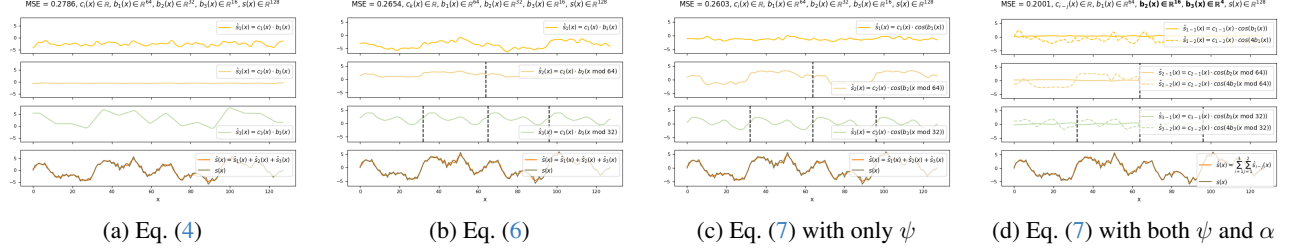


Figure 4. Visualization of different factorization methods.

of high- and low-frequency components. However, the formulation in Eq. (5) does not have such explicit harmonic feature (coefficient and basis are learned maps), and thus as in Fig. 4 we witness performance loss due to lack of such guidance. Inspired by position encoding [7, 9, 11, 65, 68] and Fourier feature mapping [78], we introduce coordinate transformation function  $\gamma_i$  on  $x$  before sampling basis  $b_i$ :

$$\hat{I}(x) = \mathcal{P}\left(\text{Concat}_{i=1}^N \left\{ c_i(x) \cdot b_i(\gamma_i(x)) \right\}\right). \quad (6)$$

In practice, we empirically[12] use sawtooth transformation  $\gamma(x) = x \bmod k, k \in \mathbb{R}$ , visualized in Fig. 2.a. We argue that the function explicitly imposes patch-like periodic constraints and, therefore, enforces models to learn such repetitive patterns.

**Multi-frequency Modulation.** [72] has shown that neural networks are biased towards learning low-frequency content. Hence, we propose multi-frequency modulation to compel the model to fit high-frequency components, visualized in Fig. 4:

$$\hat{I}(x) = \mathcal{P}\left(\text{Concat}_{i=1}^N \text{Concat}_{j=1}^K \left\{ c_{ij}(x) \odot \psi(\alpha_j \cdot b_i(\gamma_i(x))) \right\}\right), \quad (7)$$

where  $\psi \in \sin, \cos$  and  $\alpha \in \mathbb{R}$ . In this way, each basis  $b_i$  contributes to both high- and low-frequency components by different values of  $\alpha$ . Consequently, if a basis is only accurate in the low-frequency domain, the output will contain undesired high-frequency noise.

Alternatively, Eq. (7) can be interpreted as making the spatial coordinates  $x, y$  in Eq. (1) learnable instead of the frequency components  $u, v$ . To validate this, we conduct experiments (Fig. 5) showing that learning coordinates mitigates the rigid constraint of uniform distribution, aligning better with the non-uniform nature of visual patterns across spatial layouts; that is, some pixels share similar RGB values, indicating smooth color transitions, while others exhibit abrupt changes, suggesting high-frequency variations.

To this end, our full Factorized Features representation is formulated in Eq. (7).

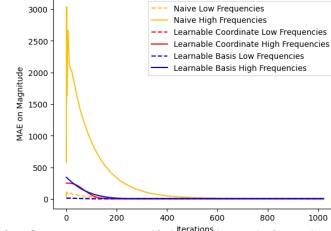


Figure 5. In this figure, we validate the claim that fixed sinusoidal functions attend more to low-frequency parts. Learnable basis denotes the **Learned Non-uniform basis** in Sec. 3.1. And we can see that Learnable Coordinate  $x$  has the same effect, verifying our conclusion.

### 3.2. Super-Resolution with Factorized Features

We represent a super-resolved image using our Factorized Features, where coefficients and basis are generated by networks  $F_{\text{coeff}}$  and  $F_{\text{basis}}$  from a low-resolution Image:

$$\hat{I}_{\text{SR}}(x) = \mathcal{P}\left(\text{Concat}_{i=1}^N \text{Concat}_{j=1}^K \left\{ c_{ij}^{\text{LR}}(x) \odot \psi(\alpha_j \cdot b_i^{\text{LR}}(\gamma_i(x))) \right\}\right), \quad (8)$$

where  $c^{\text{LR}}(x) = \text{Conv}(F_{\text{coeff}}(I_{\text{LR}}))(x)$  and  $b^{\text{LR}}(x) = F_{\text{basis}}(F_{\text{coeff}}(I_{\text{LR}}))(\gamma(x))$ . Note that we sample the outputs  $\text{Conv}(F_{\text{coeff}}(I_{\text{LR}}))$  and  $F_{\text{basis}}(F_{\text{coeff}}(I_{\text{LR}}))$  with coordinates  $x$  and  $\gamma(x)$ , respectively.

Our model comprises three main components: Coefficient Backbone  $F_{\text{coeff}}$ , Basis Swin Transformer  $F_{\text{basis}}$ , and Factorized Features Reconstruction. As shown in Fig. 3, the process begins with  $I_{\text{LR}} \in \mathbb{R}^{3 \times H \times W}$ . The Coefficient Backbone extracts features  $X_{\text{coeff}} \in \mathbb{R}^{C_c \times H_c \times W_c}$ , which are then used to generate coefficients  $c$  through convolution and pixel shuffle operations. Then,  $X_{\text{coeff}}$  is fed into the Basis Swin Transformer to produce a multi-scale basis  $b = \{b_1, \dots, b_N\}$ ,  $b_i \in \mathbb{R}^{C_{b_i} \times H_{b_i} \times W_{b_i}}$ . The coefficients and basis are combined to reconstruct  $I_{\text{SR}} \in \mathbb{R}^{3 \times sH \times sW}$  using Eq. (8), where  $s$  is the scale factor.

We optimize model parameters using  $L_1$  loss.

To demonstrate the effectiveness of our method, we use existing SR methods [16, 17, 91] as the Coefficient Backbone. For the Basis Swin Transformer, we employ simple Swin Transformer Blocks [59] with a series of special downsampling operations. Specifically, we use a dilation-

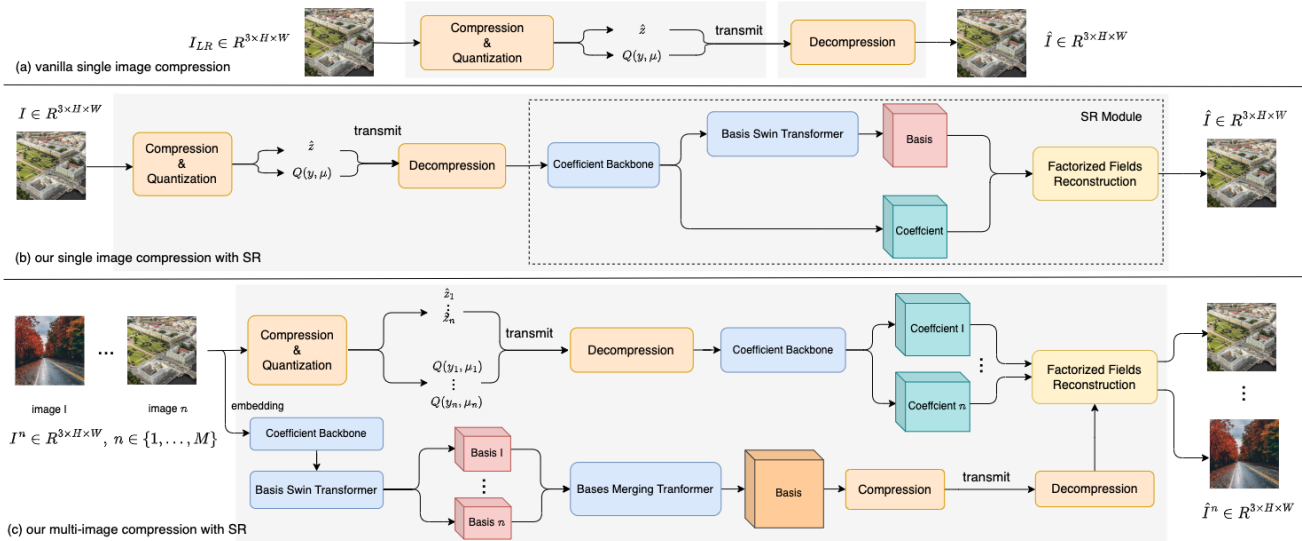


Figure 6. **The illustration of our joint image-compression and super-resolution framework compared with the traditional compression-only method.** (a) Traditional learning-based compression methods. (b) Our approach surpasses (a) by incorporating our Super-Resolution (SR) Module from Sec. 3.2 as information-recovery prior, detailed in Sec. 3.3 (c) Expanding on (b), Sec. 3.3.1 introduces a multi-image compression strategy that utilizes both our SR Module and a Basis Merging Transformer to capture shared structure.

like downsampling technique (Fig. 2.c) to accommodate the sawtooth sampling pattern. The final basis is refined using additional upsampling and convolution layers.

### 3.3. Image Compression with Factorized Features

Image Compression, at its core, is to strike a balance between the amount of information contained in the latent bits and the final image quality. However, as discussed in Sec. 1 and Sec. 2, most recent works draw emphasis on how to retrieve implicit elements through designing different architectures, such as analysis transforms and entropy models [39, 44], or decomposition modules [24, 75], while this paper aims at addressing the representation itself to better capture the structural correlations and thus achieve better image quality through Factorized Features formulation as in Eq. (7)

**Priors from SR.** In addition, with our trained SR model described in Sec. 3.2, it intuitively serves as a strong prior for information recovery, i.e., it contains extensive knowledge of how to reconstruct missing details and enhance image quality by leveraging learned patterns from the training data. Thus, since Super-Resolution and Image Compression share the core principle of reconstructing and enhancing image details from low-quality sources, we can effectively integrate this prior into the compression pipeline.

The overall pipeline is shown in Fig. 6b. To demonstrate the robustness of our representation and the effectiveness of the SR prior, the compression and decompression networks greatly follow [55], with only the synthesis transform replaced by our SR pipeline, where the details can be referenced in Supplementary Materials. In practice, the train-

ing is performed in two stages. After we obtain the trained SR prior, the model is fine-tuned with a lower learning rate alongside the compression module, which is then trained end-to-end with the loss function defined as

$$L = R(\hat{y}) + R(\hat{z}) + \lambda \cdot D(x, \hat{x}), \quad (9)$$

#### 3.3.1. Multi-Image Compression

For each basis  $b_i \in \mathbb{R}^{C_{b_i} \times H_{b_i} \times W_{b_i}}$  associated with any arbitrary image, we can consider it as encapsulating the inherent pixel structure. These bases can be combined into a unified generic basis that captures the structural distribution of images and potentially reduces noise. Given  $M$  images and their respective bases  $b_i^n, n \in \{1, \dots, M\}$ , we apply a Basis Merging Transformer  $F_{\text{merge}}$  at each location to integrate the  $M$  elements:

$$b_i(h, w) = F_{\text{merge}}(\{b_i^n(h, w) \mid n \in 1, \dots, M\}), \quad (10)$$

where  $0 \leq h < H_{b_i}$ ,  $0 \leq w < W_{b_i}$ ,  $F_{\text{merge}}$  is a standard transformer, similar in architecture to that described in [70]. We treat the bases as tokens and prepend the sequence with a  $CLS$  token, concluding the sequence to form the final merged basis.

Since compression induces error, according to Fig. 6b, the Coefficient feature map  $X_{\text{coeff}}$  generated with Coefficient Backbone contains misinformation, and Basis Swin Transformer that uses such features would capture the information wrongfully for the basis and thus amplify error. To solve this, we exploit the mergeable property of basis, compress and transmit the merged basis independently along

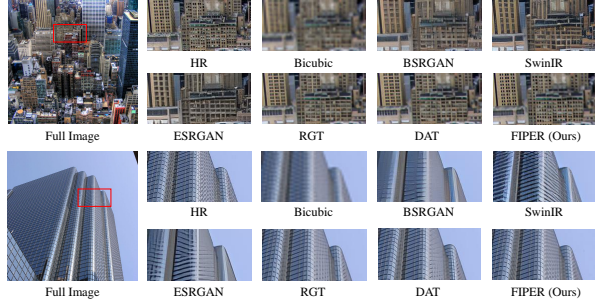


Figure 7. **Visual comparisons on super-resolution (4 $\times$ )**. The proposed method achieves the best reconstruction results to the reference HR images.

other quantized variables  $\{Q(y, \mu), \hat{z}\}$ , and finally reconstruct the  $M$  images with the merged basis and their individual decoded coefficients. as illustrated in Fig. 6c. This way, we can enjoy less information loss with basis while maintaining low bit rates.

## 4. Experiments

### 4.1. Image Super-Resolution

**Experimental Setup.** We conduct extensive experiments to validate the effectiveness of our Factorized Features representation for Super-Resolution tasks. Following the strategy outlined in [15] and [20], we adapt the same-task pre-training approach for all the Super-Resolution models. Unlike these previous works, we leverage the SA-1B dataset from [37], which includes approximately 10 million images, where we randomly sample 4 million for training, which is much less than that of ImageNet [22], which is used for [15] and [20] pretraining. Note that we use SA-1B just for its content-rich and high-resolution images since SA-1B is designed for training segmentation models, whereas ImageNet focuses primarily on single-class prediction. We further conduct experiments to compare training performance with SA-1B and ImageNet in Tab. 1. While the performances are mostly equivalent, we witness faster convergence with SA-1B during training.

To be more focused on the representation itself, we utilize various pre-trained SR models (SwinIR [48], HAT [16], DAT [17], and ATD [92]) as the Coefficient Backbone, with a consistent Basis Transformer architecture. Training involves initializing the Coefficient Backbones from pre-trained SR models and randomly initializing the Basis Transformers. Models are pre-trained for 300k iterations on the SA-1B dataset. After pretraining, we use DF2K (DIV2K [1] + Flickr2K [52]) as the finetuning dataset following [15, 21] for 200k iterations.

For pretraining, we utilize AdamW optimizer with learning rate  $2e-4$ , batch size 32, betas (0.9, 0.99), and other

parameters set to PyTorch default, while we use learning rate  $1e-5$  during finetuning. Throughout training, the input is randomly cropped to  $256 \times 256$  and bicubically resized to  $64 \times 64$  for Coefficient Backbone input. As for the hyperparameter of Factorized Features, the number  $N$  of coefficient and basis is set to 6, and the scalars  $\alpha_j$  are set to  $\{1, 4, 16, 64\}$  since we want to capture both base frequency  $\alpha_j = 1$  and high frequency  $\alpha_j = 64$  information. More implementation details can be found in supplementary materials.

**Quantitative Results.** Tab. 1 presents the quantitative comparison between our approach and state-of-the-art (SoTA) methods. We evaluate the methods using five benchmark datasets, including Set5 [6], Set14 [90], BSD100 [63], Urban100 [33], and Manga109 [64]. For quantitative metrics, PSNR and SSIM are reported. The average relative improvement of **204.4%** in PSNR over the baseline across the five datasets is calculated using the formula  $(c - b)/(a - b)$ , where  $b$  represents the PSNR of a representative baseline, SwinIR,  $a$  represents the PSNR of SOTA, HAT-L, and  $c$  represents the PSNR of our best model, HAT-L-F. This formula measures the relative performance gain of our model compared to the gap between HAT-L and SwinIR.

To validate the effectiveness of our framework, we employ three different SoTA SR models—ATD [91], DAT [17], and HAT [16]—as the Coefficient Backbone in our pipeline, which we denote as ATD-F, DAT-F, and HAT-F, respectively. These models exhibit significant improvements when compared to their counterparts, ATD-L, DAT-L, and HAT-L, which possess similar parameter counts. It is important to note that only [16] provides a large-scale model. To maintain fairness, we scale up ATD and DAT to match this size and train them under the same configuration as our model, including both pretraining and fine-tuning stages. To ensure an equitable comparison with other methods, we further train another model, HAT-F-ImageNet, using ImageNet as the pretraining dataset, following the protocols outlined in [14, 16]. The results demonstrate that its performance remains consistent with only minor perturbations.

Furthermore, in traditional Fourier Series and other image processing methods [82], the basis is typically derived first and then used to compute the coefficients. In contrast, our method derives the coefficient features first, as illustrated in Fig. 3. To explore this difference, we develop another variant of our model, denoted HAT-F-Basis-First, where we reverse the order of operations. In this case, we first pass the image through the Basis Swin Transformer and then use the resulting basis features and the image input to derive the coefficients. This approach, however, leads to a gigantic performance drop, showing the importance of the order of the pipeline. Specifically, we argue that in our pipeline, the Coefficient Backbone functions more as a feature extraction module, where the refined features facilitate

Table 1. **Quantitative comparisons on 4× super-resolution with state-of-the-art methods.** The best results are colored **red**. The models with † are those who use same-task pretraining [16]. Please refer to **quantitative results** in Sec. 4.1 for details.

Method	Params	MACs	Forward Pass	Set5		Set14		B100		Urban100		Manga109	
	(M)	(G)	Memory (MB)	PSNR↑	SSIM↑								
SwinIR [48](ICCV2021W)	28.01	119.68	3,826	32.93	0.9043	29.15	0.7958	27.95	0.7484	27.56	0.8273	32.22	0.9273
ATD [92](CVPR2024)	20.26	77.10	6,572	33.14	0.9061	29.25	0.7976	28.02	0.7524	28.22	0.8414	32.65	0.9308
DAT [17](ICCV2023)	14.80	61.66	4,192	33.15	0.9062	29.29	0.7983	28.03	0.7518	27.99	0.8365	32.67	0.9301
RGT [18](ICLR2024)	13.37	834.25	3,404	33.16	0.9066	29.28	0.7979	28.03	0.7520	28.09	0.8388	32.68	0.9303
HAT <sup>†</sup> [15](CVPR2023)	20.77	86.02	3,692	33.18	0.9073	29.38	0.8001	28.05	0.7534	28.37	0.8447	32.87	0.9319
HAT-L <sup>†</sup> [15](CVPR2023)	40.84	167.27	6,804	33.30	0.9083	29.47	0.8015	28.09	0.7551	28.60	0.8498	33.09	0.9335
ATD-L <sup>*</sup>	49.42	184.83	15,582	33.12	0.9062	29.31	0.7985	28.02	0.7514	28.25	0.8422	32.78	0.9309
DAT-L <sup>*</sup>	43.01	175.42	11,326	33.33	0.9084	29.40	0.8009	28.04	0.7543	28.49	0.8473	33.02	0.9321
ATD-F <sup>†</sup> (Ours)	45.46	149.87	8,674	33.29	0.9082	29.48	0.8017	28.03	0.7539	28.53	0.8487	33.11	0.9335
DAT-F <sup>†</sup> (Ours)	40.00	134.42	6,206	33.45	0.9094	29.60	0.8039	28.13	0.7560	28.75	0.8520	33.23	0.9339
HAT-F <sup>†</sup> (Ours)	45.97	158.79	5,750	33.53	0.9100	29.65	0.8050	28.18	0.7569	28.79	0.8527	33.33	0.9342
HAT-F-ImageNet <sup>†</sup> (Ours)	45.97	158.79	5,750	33.55	0.9102	29.63	0.8049	28.18	0.7569	28.80	0.8529	33.33	0.9342
HAT-L-F <sup>†</sup> (Ours)	66.04	240.03	8,888	<b>33.75</b>	<b>0.9116</b>	<b>29.87</b>	<b>0.8091</b>	<b>28.31</b>	<b>0.7597</b>	<b>29.51</b>	<b>0.8637</b>	<b>33.36</b>	<b>0.9343</b>
HAT-F-Basis-First <sup>†</sup> (Ours)	46.67	161.66	5,696	33.33	0.9085	29.47	0.8015	28.10	0.7554	28.57	0.8494	33.14	0.9336
HAT-F-Concat <sup>†</sup> (Ours)	45.52	129.05	4,826	33.46	0.9095	29.57	0.8035	28.16	0.7566	28.73	0.8518	33.28	0.9341

downstream basis extraction.

Lastly, to evaluate the effectiveness of our Factorized Features, we trained a model named HAT-F-Concat, which does not apply the formulation in Eq. (7). Instead, it concatenates the basis and coefficient directly and decodes the resulting features to produce the output. Although this approach results in reduced performance, which indicates the representation does act as an imperative role in modeling image information, the Basis Swin Transformer with Sawtooth downsampling still contributes to improved reconstruction, even without Factorized-Fields decoding, highlighting its effectiveness.

**Visual Comparison.** We provide the visual comparison in Fig. 7. The images are randomly sampled from the DIV2K dataset. Our method faithfully reconstructs the image details, whereas the other approaches suffer from over-smoothing or hallucinating details absent in the ground truth.

**Multi-frame SR.** Due to space limitations, we provide additional comparisons on multi-frame SR in the supplementary materials.

## 4.2. Single- and Multi-Image Compressions

**Experimental Setup.** We evaluate our Factorized Features for image compression tasks against state-of-the-art methods. Following the Super-Resolution setup in Sec. 4.1, we train on the SA-1B dataset. To emphasize our representation, compression and decompression modules are initialized from pre-trained models [55], then fine-tuned end-to-end on 256×256 patches for 200k iterations using the AdamW optimizer [60] (learning rate=1e-5, batch size=16, betas=(0.9, 0.99)).

Table 2. **Comprehensive evaluation for image compression.** Using VTM as an anchor for calculating BD-Rate. Latencies are measured under an NVIDIA GTX 3090 GPU.

Method	BD-Rate (%) ↓	Latency(s)		Params(M)
		Tot Enc ↓	Tot Dec ↓	
VTM	0.00	129.21	0.14	-
Xie (MM'21)	-0.78	2.93	6.00	50.0
Cheng (CVPR'22)	5.44	1.98	4.69	29.6
STF (CVPR'22)	-4.31	0.14	0.13	99.9
ELIC (CVPR'22)	-7.24	0.07	0.09	36.9
TCM (CVPR'23)	-11.74	0.16	0.15	76.7
CCA (Neurips'24)	-20.97	0.11	0.09	64.9
TCM-HAT-L-F (Ours)	-21.09	0.109	0.264	110.34
TCM-HAT-F-multi M=1 (Ours)	27.96	0.232	0.174	131.35
TCM-HAT-F-multi M=2 (Ours)	2.70	0.232	0.174	131.35
TCM-HAT-F-multi M=4 (Ours)	-10.11	0.232	0.174	131.35
TCM-HAT-F-multi M=8 (Ours)	-16.61	0.232	0.174	131.35
TCM-HAT-F-multi M=16 (Ours)	-19.88	0.232	0.174	131.35
TCM-HAT-F-multi M=24 (Ours)	-20.97	0.232	0.174	131.35

We integrate our SR Module with the pre-trained compression module TCM, creating TCM-HAT-F and TCM-HAT-L-F models. TCM-HAT-F-multi represents the multi-image compression pipeline. For multi-image compression in Fig. 6.c, we set the Basis Swin Transformer and the Basis Merging Transformer to be trainable while the other parts remain frozen.

**Rate-Distortion Performance Comparison.** We compare our model with State-of-the-Art learned end-to-end image compression algorithms, including [56], [13], [98], [87], [19], [3], [44], [34], [66], [5], [71], and [32]. The classical image compression codec, VVC [80], is also tested by using VTM12.1. The rate-distortion performance on various datasets, including Kodak, Tecnick's old test set with resolution 1200×1200, and CLIC Professional Validation, is shown in Fig. 8.

In Tab. 2, our TCM-HAT-L-F model achieved a signifi-

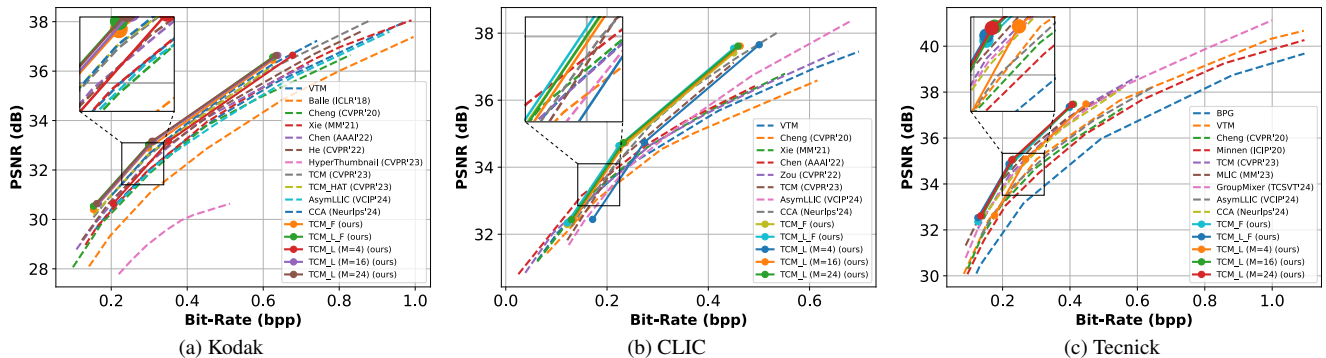


Figure 8. Performance (RD-Curve) evaluation on image compression using different datasets.

Table 3. Validation of the effectiveness of SR prior. The best PSNRs are marked in red.

Method	Kodak						CLIC						Tecnick					
	$\lambda = 0.0025$		$\lambda = 0.0067$		$\lambda = 0.025$		$\lambda = 0.0025$		$\lambda = 0.0067$		$\lambda = 0.025$		$\lambda = 0.0025$		$\lambda = 0.0067$		$\lambda = 0.025$	
	bpp	PSNR $\uparrow$	bpp	PSNR $\uparrow$	bpp	PSNR $\uparrow$	bpp	PSNR $\uparrow$	bpp	PSNR $\uparrow$	bpp	PSNR $\uparrow$	bpp	PSNR $\uparrow$	bpp	PSNR $\uparrow$	bpp	PSNR $\uparrow$
TCM[55]	0.1533	30.0834	0.2983	32.5841	0.6253	36.1345	0.1214	31.8207	0.2235	34.2098	0.4503	37.1201	0.1268	32.0588	0.2193	34.3669	0.3981	36.9066
TCM-HAT-F-Scratch	0.1570	30.0857	0.2976	32.5893	0.6211	36.1389	0.1214	31.9421	0.2235	34.2894	0.4503	37.1434	0.1258	32.0632	0.2189	34.3781	0.4001	36.9223
TCM-HAT	0.1567	30.1843	0.2992	32.6454	0.6268	36.2267	0.1220	31.9737	0.2266	34.3319	0.4512	37.2486	0.1262	32.1423	0.2174	34.5124	0.3971	36.9934
TCM-HAT-F	0.1574	<b>30.4012</b>	0.2998	<b>32.8910</b>	0.6276	<b>36.4461</b>	0.1229	<b>32.1917</b>	0.2249	<b>34.4109</b>	0.4512	<b>37.3135</b>	0.1255	<b>32.4591</b>	0.2186	<b>34.7656</b>	0.3975	<b>37.3244</b>

Table 4. Comparison of improvements of Factorized Features.  $\psi$  and  $\alpha$  are the same in Eq. (8).

Metric	PSNR $\uparrow$	SSIM $\uparrow$	LPIPS $\downarrow$
Baseline [12]	22.04	0.505	0.5296
Ours	38.44	0.999	0.0385
No $\psi$ to control magnitude	13.46	0.147	0.766
No $\alpha$ for pixel-wise frequency information	21.25	0.537	0.527

cant BD-Rate improvement of -21.09% compared to VTM, outperforming previous state-of-the-art methods. The multi-image compression approach (TCM-HAT-F-multi) shows increasing performance gains with the number of images compressed simultaneously, reaching -20.97% BD-Rate improvement for  $M = 24$ . The result shows that direct transmission of bases would reduce the error from Co-efficient Backbone to Basis Swin Transformer and that the distortion increases with  $M$ , as the information contained in the merged basis is limited, and merging multiple bases into one would cause increasing information loss.

Our experiments validate the effectiveness of FIPER in image compression, demonstrating substantial improvements across benchmarks (Kodak, CLIC, Tecnick). The multi-image compression strategy particularly excels with larger image sets, highlighting strong scalability. Additionally, our method achieves competitive latency, significantly improving compression efficiency while balancing quality and speed.

### 4.3. Ablation Studies

**Influence of SR Priors in Image Compression.** We conduct experiments with various configurations to verify our image compression pipeline’s effectiveness. TCM-HAT

refers to using the original HAT [16] instead of our SR Module in Fig. 6b. TCM-HAT-F represents our full pipeline, while TCM-HAT-F-Scratch initializes the SR Module randomly. Results demonstrate that integrating SR priors improves image compression performance, and our representation further enhances results, highlighting the robustness of Factorized Fields.

**Effectiveness of Factorized Features Design.** We conduct experiments to verify our multi-frequency modulation. The quantitative performance reported on single-image regression is shown in Tab. 4, where each result is measured after 256 iterations. Compared to baseline results, our refinements in modeling pixel-level frequency have significantly improved all performance metrics. Additionally, our results demonstrate that the modulation function  $\psi$  and the scalar  $\alpha$  are interdependent, each essential to the other’s function.

## 5. Conclusion

We proposed Factorized Features, a representation that decomposes images into multi-frequency components to model implicit structures and patterns. Our approach addresses challenges in Super-Resolution and Image Compression by effectively restoring details and preserving visual fidelity. We integrate SR priors with Image Compression for better information recovery and introduce a basis-merging technique to enhance multi-image processing performance.

**Limitations.** Although effective, our method requires further optimization for computation-limited scenarios such as real-time decoding. Additionally, incorporating semantic information remains a promising direction for future research.

# FIPER: Generalizable Factorized Features for Robust Low-Level Vision Models

## Supplementary Material

### A. Overview

This supplementary material provides additional implementation details and experimental results to complement our main manuscript. Specifically, we first elaborate on the background of factor fields and learned image compression in Appendix B, which were omitted in the main paper due to space limitations. Next, in Appendix D, we present comprehensive details about the benchmarks, including the Video Super-Resolution task, which was not discussed in the main paper. Finally, we provide extensive visualizations to facilitate a more detailed comparison of the results in Appendix H.

### B. Preliminaries

In this section, we briefly introduce the background of the factor fields [12], and Learned Image Compression along with their properties.

**Factor Fields.** The concept of decomposition fields or factorized matrices in the reconstruction of 2D images or 3D scenes has shown superior rendering quality and improved efficiency recently [7, 9, 11, 26, 27, 68], while [12] first proposed a unified representation called factor fields. For a 1D signal  $s(x)$ , the factor fields formulation is:

$$\hat{s}(x) = c(x)^T b(\gamma(x)), \quad (11)$$

where  $c(x) = (c_1(x), \dots, c_N(x))^T$  are spatial-varying coefficient fields,  $b(x) = (b_1(x), \dots, b_N(x))^T$  are basis functions, and  $\gamma(x)$  is a coordinate transformation. The coefficient and basis are queried by sampling with the coordinates  $x$ . This generalizes to Q-dimensional signals:

$$\hat{s}(x) = \mathcal{P}(c(x) \odot b(\gamma(x))), \quad (12)$$

where  $\mathcal{P}$  is a projection function and  $\odot$  denotes the element-wise product. In practice, for multi-dimensional coefficients:

$$\hat{s}(x) = \mathcal{P}\left(\text{Concat}_{i=1}^N \left\{ c_i(x) \odot b_i(\gamma_i(x)) \right\}\right). \quad (13)$$

This formulation allows the same basis to be applied at multiple spatial locations while varying the coefficients, especially when  $\gamma$  is a periodic function.

**Learned Image Compression.** Following [3, 66], a learned image compression model with a channel-wise en-

tropy model can be formulated as:

$$\begin{aligned} z &= h_a(y; \phi_h), \quad y = g_a(x; \phi), \\ \{X_{\text{mean}}, X_{\text{scale}}\} &= h_s(\hat{z}; \theta_h), \quad \hat{z} = Q(z), \\ \hat{y} &= \{Q(y_0 - \mu_0) + \mu_0, \dots, Q(y_t - \mu_t) + \mu_t\}, \\ \hat{x} &= g_s(\bar{y}; \theta), \quad \bar{y} = \text{Refine}_{\theta_r}(\mu_0, \dots, \mu_t, \hat{y}), \end{aligned} \quad (14)$$

where  $0 \leq t < l$ ,  $\mu_t = e_i(\hat{y}_{<i}, X_{\text{mean}})$ . The encoder  $g_a$  transforms the raw image  $x$  into a latent representation  $y$ . A hyper-prior encoder  $h_a$  further processes  $y$  to output  $z$ , capturing spatial dependencies.  $z$  is then quantized to  $\hat{z}$ , where a factorized density model  $\varphi$  is used to encode quantized  $\hat{z}$  as  $p_{z|\varphi}(\hat{z} | \varphi) = \prod_j (p_{z_j|\varphi}(\varphi) * \mathcal{U}(-\frac{1}{2}, \frac{1}{2}))(\hat{z}_j)$  where  $j$  specifies the position or each element of each signal. The derivation of the equation can be found in [2]. Next,  $\hat{z}$  is decoded by  $h_s$  to produce features  $X_{\text{mean}}$  and  $X_{\text{scale}}$ , used to estimate the mean  $\mu$  and variance  $\sigma$  of  $y$ . The latent  $y$  is divided into  $l$  slices, and each quantized around computed means  $\mu_t$ . These means are derived from earlier quantized slices and  $X_{\text{mean}}$  by a slice network  $e_i$ . The quantized slices form  $\hat{y}$ . For decompression,  $\hat{y}$  is refined using  $\text{Refine}_{\theta_r}$ , based on  $\mu_t$  and  $\hat{y}$  to produce  $\bar{y}$ , approximating the original  $y$ . Finally,  $g_s$  reconstructs the decompressed image  $\hat{x}$  from  $\bar{y}$ . The model is trained using a Lagrangian multiplier-based rate-distortion optimization:

$$\begin{aligned} L &= R(\hat{y}) + R(\hat{z}) + \lambda \cdot D(x, \hat{x}) \\ &= \mathbb{E}[-\log_2(p_{\hat{y}|\hat{z}}(\hat{y} | \hat{z}))] + \mathbb{E}[-\log_2(p_{z|\varphi}(\hat{z} | \varphi))] \\ &\quad + \lambda \cdot \mathcal{D}(x, \hat{x}) \end{aligned} \quad (15)$$

where  $R(\hat{y})$  and  $R(\hat{z})$  denote bit rates,  $D(x, \hat{x})$  is the distortion term (calculated by MSE), and  $\lambda$  balances compression efficiency and image fidelity. In our experiments, we follow [55], modifying only  $g_s$  to demonstrate our representation’s effectiveness.

### C. Differences from Factor Fields.

We explicitly highlight how **sawtooth-based sampling** and **multi-frequency modulation** extend the original factor fields. In our 1D and 2D toy examples as shown in Figs. 9 and 10, traditional SR/IC representations can be viewed as a “vanilla” scenario with  $N = 1$  and  $c(x) = 1$ . Factor fields already improve accuracy over such baselines, but our introduction of  $\psi$  and  $\alpha$  further captures both high- and low-frequency details. Specifically, forcing  $\alpha = 4$  compels the network to learn broader frequency ranges and avoid noise from the fixed modulation. To confirm these advantages, we trained *smaller SR models* and compared

them with factor fields in Tab. 5. The results illustrate that our multi-frequency constraint yields significant gains even in simpler configurations, underscoring its importance for high-frequency detail preservation and overall reconstruction quality.

## D. Implementation Details

**Single Image Super-Resolution** The architecture of our SR networks is shown in Fig. 11. Firstly, for Coefficient Backbones from various pre-trained models like [15, 17, 91], we replace the output upsampling layer (mostly pixel shuffle) with convolution of channel  $D = 256$ , i.e., for input image with resolution  $64 \times 64$ , the original pre-trained models process hidden states in  $64 \times 64$ , and then upsample the output to  $256 \times 256$  for final result, where we replace the upsampling with convolution and output the final hidden state  $X_{coeff} \in R^{256 \times 64 \times 64}$ .

Next, the Basis Swin Transformer begins with feature embedding, extending the channels  $D$  from 256 to 384, where the features are then passed through a series of SwinV2[59] and Sawtooth-Aware Downsampling Blocks. Specifically, each block contains two layers, one of which uses shifted window attention. After each block, the hidden state goes through upsampling by 4x and convolution to convert the output basis channel to 24. Then, the Sawtooth-Aware Downsample block rearranges the hidden state  $h$  as discussed in the main paper, which can be viewed as:

$$h = \text{rearrange}(h, 'b c (s h) (s w) \rightarrow b (s s c) h w'), s = 2 \quad (16)$$

, and reduces the feature channel by 4. In all experiments we use  $N = 6$ , i.e. there are 6 bases, where  $Basis_i \in R^{24 \times \frac{256}{2^i} \times \frac{256}{2^i}}$  for  $i$  in  $\{0 \dots 5\}$ .

Finally, we derive our Coefficient by a series of Convolution and Pixelshuffle layers and decoded the Bases and Coefficient to a predicted high-resolution image by Eq. (17):

$$\hat{I}(x) = \mathcal{P} \left( \text{Concat}_{i=1}^N \left\{ c_i(x) \odot \psi(\alpha_j \cdot b_i(\gamma_i(x))) \right\} \right). \quad (17)$$

In practice, the coefficient is generated with channels equal to the total number of base channels, and it is split accordingly by channels.

**Multi-Image (Video) Super-Resolution** Building upon our prior work in Single-Image Super-Resolution (SISR), we extend the applicability of Factorized Features to tackle the challenges in Multi-Image Super-Resolution (MISR). In the main paper, we introduced the Basis Merging Transformer for Multi-Image Compression. Here, we further expand its functionality to generate per-timestamp Coefficients and Bases.

To evaluate the effectiveness of our approach, we use Video Super-Resolution (VSR) as the benchmark task.

Specifically, we simply leverage transformer blocks from [70] to model temporal correlations. For a given video, we first derive the Coefficient and Basis for each frame and rearrange each level  $i$  of the Coefficients or Basis such that the spatial dimensions  $H$  and  $W$  are treated as the batch dimension, while the temporal dimension is processed as a sequence of tokens for the Transformer. Next, we apply positional embedding to the tokens, process the tokens with the transformer blocks, and finally decode the Coefficient and Basis token from the respective position with convolution layers for the output super-resolved frames.

Tab. 6 shows quantitative comparison with state-of-the-art methods. All VSR experiments were conducted using bicubic 4X downsampling. The training dataset includes the REDS[69] and Vimeo-90K[89] datasets, while the testing dataset comprises REDS4[69], Vid4[53], and Vimeo-90K-T[89].

For the REDS dataset, we train for 300k iterations using 16 input frames, with a learning rate of  $1e-4$  and a cosine learning rate that gradually decays to  $1e-7$ . The batch size is set to 8, and the Coefficient Backbone and the Basis Swin Transformer are initialized from SISR. When training on the Vimeo-90K dataset, we first conduct 300k iterations with 14 input frames with flip sequence, we then train model on 7 input frames with flip sequence, using a learning rate of  $1e-4$  and a cosine learning rate decay to  $1e-7$ . We initialize the weights using the model trained on the REDS dataset. The batch size remains 8. Note that the training is only conducted on the newly added transformer blocks, i.e., the Coefficient Backbone and Basis Swin Transformer are frozen. Test results for the REDS model are reported on the REDS4 dataset, while test results for the Vimeo-90K model are reported on Vimeo-90K-T and Vid4. We calculate PSNR and SSIM on the RGB channel for REDS4 and Y channel for Vimeo-90K-T and Vid4, following previous work[49, 74, 88].

**Single Image Compression** As discussed in the main paper, to make a fair comparison with the state-of-the-art, our entropy model and compression backbone greatly follow that of [55], as shown in Fig. 12 (more details can be found in [55]). What we do here is that we use the output from the last main layer and convert it to match the hidden channel of the SR Module.

**Multi-Image Compression** Following VSR, we use transformer blocks to merge the bases. The difference here is that we additionally prepend a CLS token so that we can use it as the final merged basis. For the merged basis compression, we utilize the same architecture of the image branch, i.e., we randomly initialize a module from [55] with input and out channels change. After the Basis Merging Transformer is trained, we follow the same training set-

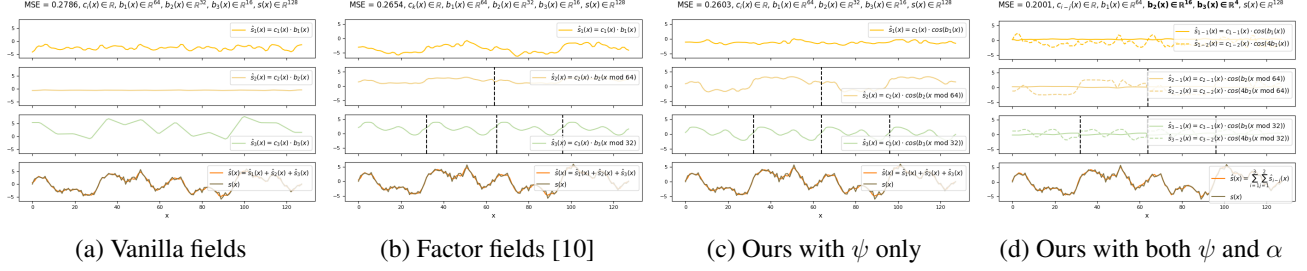


Figure 9. 1D toy example.



Figure 10. 2D toy example.

ting for Basis compression while randomly sampling 1 to 24 images for a batch and setting only the Basis compression module trainable.

### E. Merged-Basis Strategy & SR Priors.

The SR prior accelerates detail recovery by leveraging high-resolution knowledge while basis merging exploits shared structures for efficiency. Since merging is introduced *after*, the compression model is pre-trained, and improvements stem not only from the SR prior but also from the well-initialized basis merging. When trained from scratch (see Tab. 7), the merging transformer tends to find a universal solution rather than image-specific structures. Additionally, merging inevitably causes information loss, prompting the coefficient branch to encode more image-specific details. This mutual offset between SR prior and basis merging ultimately strengthens our approach.

### F. Encoding/Decoding Times.

Fig. 5(c) processes each of the  $M$  images through the Coefficient Backbone, Basis Swin Transformer, and Basis Merging Transformer, then compresses and transmits the merged basis. In Tab. 2, different  $M$  values primarily affect the run time of the Basis Merging Transformer. Although merging larger  $M$  increases computation, *per-image* overhead remains small once averaged by  $M$ , as shown in Tab. 8. Notably, Tab. 2 assumes each image’s basis is compressed independently, which can be confusing. In practice, a merged basis is processed only *once*, so averaged encoding/decoding time is more realistic.

### G. Inference Time Comparison for SR.

We provide the inference time in Tab. 9, compared with extensive SR models. The inference time of different components of FIPER is also provided.

Table 5. Comparison with Factor Fields.

Method	Sawtooth	$\psi$	$\alpha$	Params	MACs	Forward Pass	Set5		Set14		B100		Urban100		Manga109	
	$\gamma(x)$			(M)	(G)	Memory (MB)	PSNR $\uparrow$	SSIM $\uparrow$								
HAT-S				9.62	40.38	3,214	32.92	0.9047	29.15	0.7958	27.97	0.7505	27.87	0.8346	32.35	0.9283
HAT				20.77	86.02	3,692	33.04	0.9056	29.23	0.7973	28.00	0.7517	27.97	0.8368	32.48	0.9292
HAT-FA-Small	✓			15.99	57.61	3,678	33.06	0.9065	29.26	0.7976	28.04	0.7524	28.12	0.8413	32.52	0.9301
HAT-F-Small-only-sin	✓	{sin}	{1, 4, 16, 64}	16.13	66.34	4,176	33.16	0.9067	29.33	0.7989	28.05	0.7530	28.26	0.8429	32.64	0.9312
HAT-F-Small-half-freq	✓	{sin, cos}	{1, 16}	16.13	66.34	4,148	33.18	0.9073	29.35	0.8003	28.02	0.7521	28.31	0.8431	32.70	0.9316
HAT-F-Small	✓	{sin, cos}	{1, 4, 16, 64}	16.26	75.06	4,640	33.24	0.9079	29.39	0.8009	28.06	0.7543	28.41	0.8453	32.82	0.9324
HAT-F (Our FIPER)	✓	{sin, cos}	{1, 4, 16, 64}	45.97	158.79	5,750	33.31	0.9085	29.45	0.8011	28.09	0.7553	28.55	0.8463	32.99	0.9330
HAT-L (ImageNet pre-trained)				40.84	167.27	6,804	33.30	0.9083	29.47	0.8015	28.09	0.7551	28.60	0.8498	33.09	0.9335

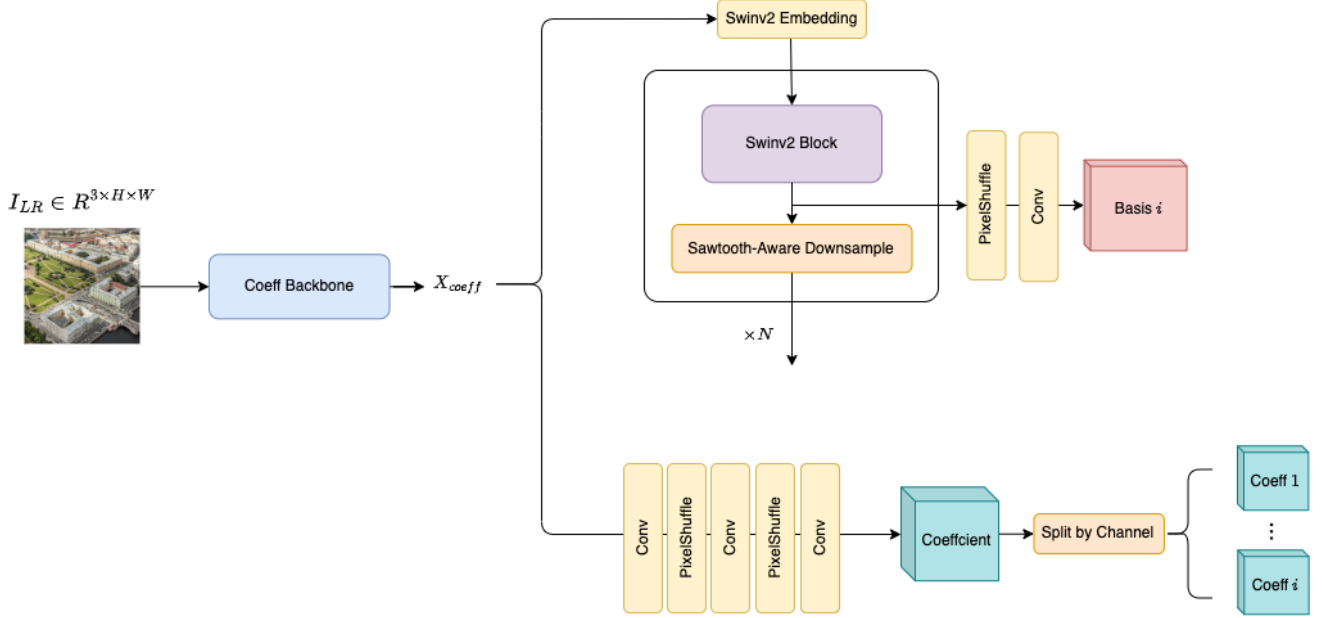


Figure 11. Detailed architecture of Super-Resolution Modules

Method	Frames	REDS4		Vimeo-90K-T		Vid4	
	REDS/Vimeo	PSNR	SSIM	PSNR	SSIM	PSNR	SSIM
BasicVSR++[10]	30/14	32.39	0.9069	37.79	0.9500	27.79	0.8400
VRT[50]	16/7	32.19	0.9006	38.20	0.9530	27.93	0.8425
RVRT[49]	30/14	32.75	0.9113	38.12	0.9527	27.99	0.8462
PSRT[74]	16/14	32.72	0.9106	38.27	0.9536	28.07	0.8485
IA-RT[88]	16/7	32.90	0.9138	38.14	0.9528	28.26	0.8517
Ours-HAT-F	16/7	32.67	0.9096	38.09	0.9512	27.95	0.8441

Table 6. Performance comparison among different methods on REDS4, Vimeo-90K-T, and Vid4 datasets. **Note that we don't use any special design on the network, such as temporal correspondence or motion sampling like previous works, demonstrating our effectiveness.**

BD-rate %	TCM-HAT-F-multi $M = 24$	TCM-HAT-F-multi $M = 24$ Coeff-Frozen	TCM-HAT-F-multi $M = 24$ Scratch
	-20.97	-19.18	-18.34

Table 7. Comparison of Merged-Basis Strategies.

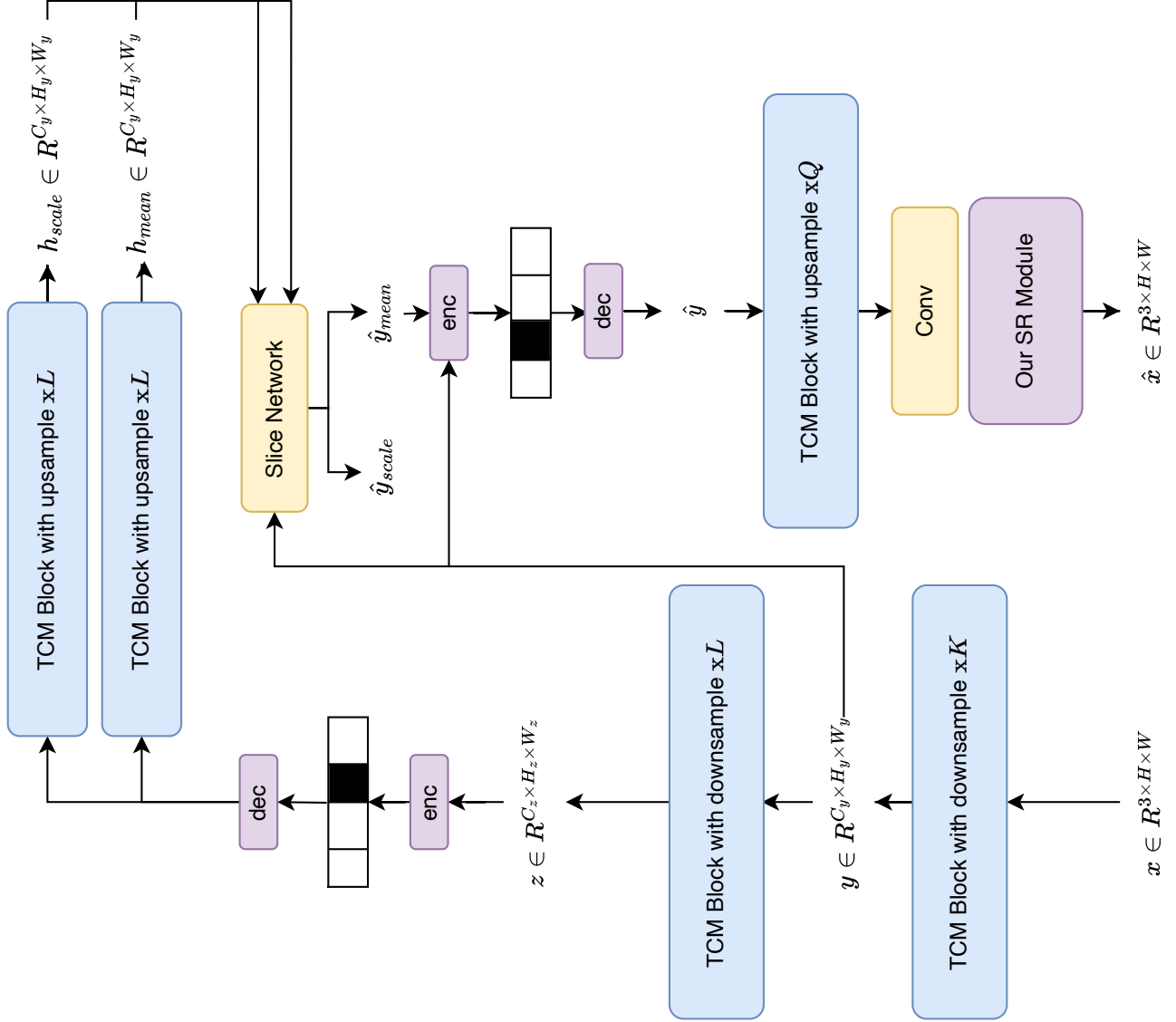


Figure 12. Detailed architecture of Compression Modules

	$M = 1$	$M = 2$	$M = 4$	$M = 8$	$M = 16$	$M = 24$
Total Basis Merging Time (sec)	0.00328	0.00628	0.01140	0.02312	0.04784	0.08064
Averaged Basis Merging Time (sec) by $M$	0.00328	0.00314	0.00285	0.00289	0.00299	0.00336
Averaged Merged Basis Compression Time (sec) by $M$	0.0645	0.0323	0.0161	0.0081	0.0040	0.0027
Averaged Merged Basis Decompression Time (sec) by $M$	0.0935	0.0467	0.0234	0.0117	0.0058	0.0039
Adjusted Enc Time (sec) by $M$	0.2320	0.1998	0.1836	0.1756	0.1715	0.1702
Adjusted Dec Time (sec) by $M$	0.1740	0.1272	0.1039	0.0922	0.0863	0.0844
BD-Rate %	27.96	2.70	-10.11	-16.61	-19.88	-20.97

Table 8. Comparison of Encoding/Decoding Times.

	HAT-S	HAT	HAT-L	ATD	DAT	RGT	HAT-F-S (Ours)	HAT-F (Ours)	HAT-L-F (Ours)	Coefficient Backbone (HAT-F)	Basis Swin Transformer (HAT-F)	Factorized Features Reconstruction (HAT-F)
Inference Time (s)	0.0387	0.0398	0.0778	0.0592	0.0594	0.0612	0.0671	0.0716	0.1084	0.0400	0.0132	0.0184

Table 9. Inference time comparison for SR.

## H. More Visualization

### H.1. Single Image Super-Resolution

Below, we provide more visual comparisons of single-image super-resolution, where FIPER denotes HAT-F.

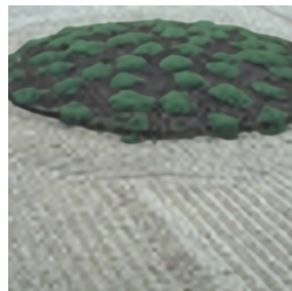
BSD100 x4 : img\_096\_SRF\_4



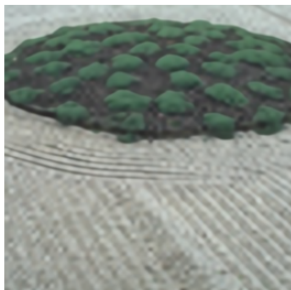
HR



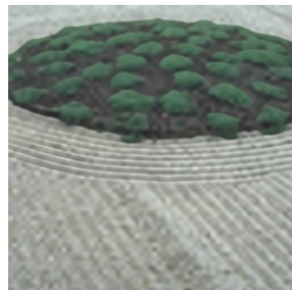
DAT



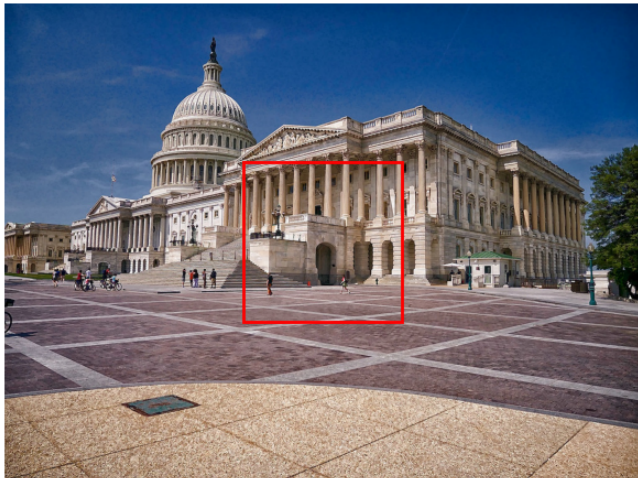
HAT-L



FIPER (ours)



Urban100 x4 : img070



HR



DAT



HAT-L



FIPER (ours)



Urban100 x4 : img046



HR



DAT



HAT-L

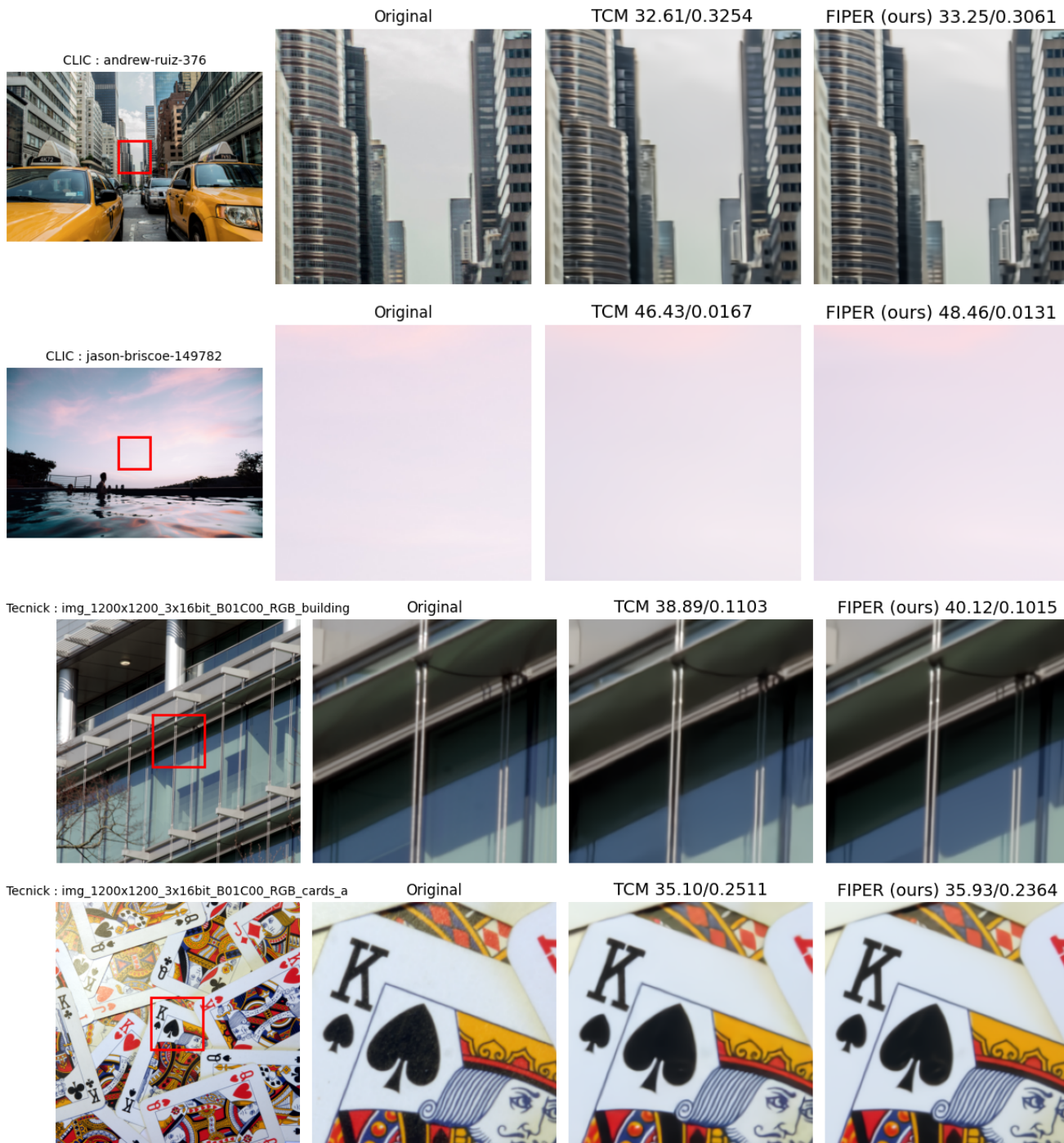


FIPER (ours)



## H.2. Image Compression

Below, we provide more visual comparisons of image compression. The results are present with TCM-HAT-F and the metrics are PSNR/Bpp.



Tecnick : img\_1200x1200\_3x16bit\_B01C00\_RGB\_cards\_b

Original

TCM 34.45/0.2274

FIPER (ours) 35.00/0.2244

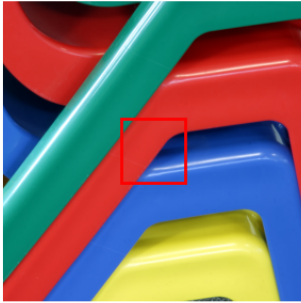


Tecnick : img\_1200x1200\_3x16bit\_B01C00\_RGB\_chairs

Original

TCM 41.77/0.0471

FIPER (ours) 42.44/0.0415

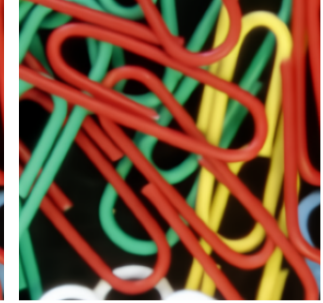
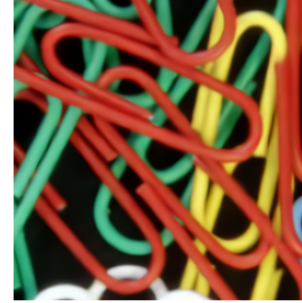
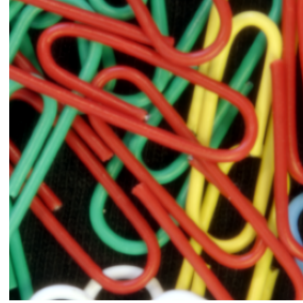


Tecnick : img\_1200x1200\_3x16bit\_B01C00\_RGB\_clips

Original

TCM 33.84/0.2909

FIPER (ours) 34.50/0.2761



Tecnick : img\_1200x1200\_3x16bit\_B01C00\_RGB\_keyboard\_a

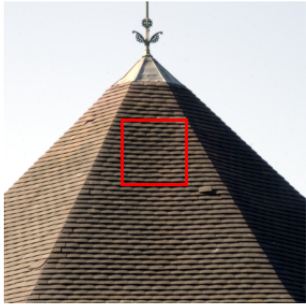
Original

TCM 35.43/0.1910

FIPER (ours) 36.06/0.1843



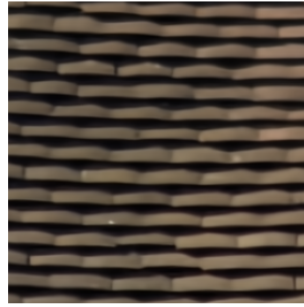
Tecnick : img\_1200x1200\_3x16bit\_B01C00\_RGB\_roof



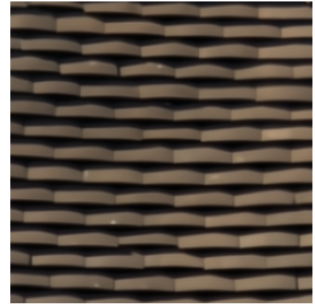
Original



TCM 35.52/0.1828



FIPER (ours) 37.02/0.1686



Tecnick : img\_1200x1200\_3x16bit\_C00C00\_RGB\_billiard\_balls\_b



Original



TCM 38.25/0.1205



FIPER (ours) 38.76/0.1171



Tecnick : img\_1200x1200\_3x16bit\_T01C00\_RGB\_pencils\_b



Original



TCM 36.61/0.1174



FIPER (ours) 37.16/0.1120



## References

- [1] Eirikur Agustsson and Radu Timofte. Ntire 2017 challenge on single image super-resolution: Dataset and study. In *The IEEE Conference on Computer Vision and Pattern Recognition (CVPR) Workshops*, 2017. 6
- [2] Johannes Ballé, David Minnen, Saurabh Singh, Sung Jin Hwang, and Nick Johnston. Variational image compression with a scale hyperprior. In *International Conference on Learning Representations*, 2018. 9
- [3] Johannes Ballé, David Minnen, Saurabh Singh, Sung Jin Hwang, and Nick Johnston. Variational image compression with a scale hyperprior. In *International Conference on Learning Representations*, 2018. 1, 7, 9
- [4] Johannes Ballé, David Minnen, Saurabh Singh, Sung Jin Hwang, and Nick Johnston. Variational image compression with a scale hyperprior. In *International Conference on Learning Representations*, 2018. 2
- [5] Fabrice Bellard. The bpg image format. <http://bellard.org/bpg/>. Last accessed on 09/20/2015. 7
- [6] Marco Bevilacqua, Aline Roumy, Christine Guillemot, et al. Low-complexity single-image super-resolution based on nonnegative neighbor embedding. In *Proceedings of the British Machine Vision Conference (BMVC)*, pages 1–10, 2012. 6
- [7] Ang Cao and Justin Johnson. Hexplane: A fast representation for dynamic scenes. In *Proceedings of the IEEE/CVF Conference on Computer Vision and Pattern Recognition*, pages 130–141, 2023. 2, 4, 9
- [8] Lahiru D. Chamain, Fabien Racapé, Jean Bégain, Akshay Pushparaja, and Simon Feltman. End-to-end optimized image compression for machines, a study. In *2021 Data Compression Conference (DCC)*, 2021. 1, 2
- [9] Eric R. Chan, Connor Z. Lin, Matthew A. Chan, Koki Nagano, Boxiao Pan, Shalini De Mello, Orazio Gallo, Leonidas Guibas, Jonathan Tremblay, Sameh Khamis, Tero Karras, and Gordon Wetzstein. Efficient geometry-aware 3D generative adversarial networks. In *arXiv*, 2021. 2, 4, 9
- [10] Kelvin CK Chan, Shangchen Zhou, Xiangyu Xu, and Chen Change Loy. Basicvsr++: Improving video super-resolution with enhanced propagation and alignment. In *Proceedings of the IEEE/CVF conference on computer vision and pattern recognition*, pages 5972–5981, 2022. 12
- [11] Anpei Chen, Zexiang Xu, Andreas Geiger, Jingyi Yu, and Hao Su. Tensorf: Tensorial radiance fields. In *European Conference on Computer Vision (ECCV)*, 2022. 2, 4, 9
- [12] Anpei Chen, Zexiang Xu, Xinyue Wei, Siyu Tang, Hao Su, and Andreas Geiger. Factor fields: A unified framework for neural fields and beyond. *arXiv preprint arXiv:2302.01226*, 2023. 2, 4, 8, 9
- [13] Fangdong Chen, Yumeng Xu, and Li Wang. Two-stage octave residual network for end-to-end image compression. In *Proceedings of the AAAI Conference on Artificial Intelligence*, 2022. 7
- [14] Hanting Chen, Yunhe Wang, Tianyu Guo, Chang Xu, Yiping Deng, Zhenhua Liu, Siwei Ma, Chunjing Xu, Chao Xu, and Wen Gao. Pre-trained image processing transformer. In *Proceedings of the IEEE/CVF conference on computer vision and pattern recognition*, pages 12299–12310, 2021. 1, 2, 6
- [15] Xiangyu Chen, Xintao Wang, Wenlong Zhang, Xiangtao Kong, Yu Qiao, Jiantao Zhou, and Chao Dong. Hat: Hybrid attention transformer for image restoration. *arXiv preprint arXiv:2309.05239*, 2023. 2, 6, 7, 10
- [16] Xiangyu Chen, Xintao Wang, Jiantao Zhou, Yu Qiao, and Chao Dong. Activating more pixels in image super-resolution transformer. In *Proceedings of the IEEE/CVF Conference on Computer Vision and Pattern Recognition (CVPR)*, pages 22367–22377, 2023. 4, 6, 7, 8
- [17] Z. Chen, Y. Zhang, J. Gu, L. Kong, X. Yang, and F. Yu. Dual aggregation transformer for image super-resolution. In *2023 IEEE/CVF International Conference on Computer Vision (ICCV)*, pages 12278–12287, 2023. 1, 2, 4, 6, 7, 10
- [18] Zheng Chen, Yulun Zhang, Jinjin Gu, Linghe Kong, and Xiaokang Yang. Recursive generalization transformer for image super-resolution. In *The Twelfth International Conference on Learning Representations*, 2024. 1, 2, 7
- [19] Zhongxue Cheng, Heming Sun, Masaru Takeuchi, and Jiro Katto. Learned image compression with discretized gaussian mixture likelihoods and attention modules. In *Proceedings of the IEEE/CVF conference on computer vision and pattern recognition*, pages 7939–7948, 2020. 1, 7
- [20] Yi-Shiuan Chou Chih-Chung Hsu, Chia-Ming Lee. Drct: Saving image super-resolution away from information bottleneck. *arXiv preprint arXiv:2404.00722*, 2023. 2, 6
- [21] Marcos V Conde, Ui-Jin Choi, Maxime Burchi, and Radu Timofte. Swin2SR: Swin2 transformer for compressed image super-resolution and restoration. In *Proceedings of the European Conference on Computer Vision (ECCV) Workshops*, 2022. 1, 2, 6
- [22] Jia Deng, Wei Dong, Richard Socher, Li-Jia Li, Kai Li, and Li Fei-Fei. Imagenet: A large-scale hierarchical image database. In *2009 IEEE Conference on Computer Vision and Pattern Recognition*, pages 248–255, 2009. 6
- [23] Chao Dong, Chen Change Loy, Kaiming He, and Xiaoou Tang. Image super-resolution using deep convolutional networks. *IEEE Transactions on Pattern Analysis and Machine Intelligence*, pages 295–307, 2014. 1, 2
- [24] Wenhong Duan, Zheng Chang, Chuanmin Jia, Shanshe Wang, Siwei Ma, Li Song, and Wen Gao. Learned image compression using cross-component attention mechanism. *IEEE Transactions on Image Processing*, 2023. 2, 5
- [25] Dahu Feng, Yan Huang, Yiwei Zhang, Jun Ling, Anni Tang, and Li Song. A generative compression framework for low bandwidth video conference. In *2021 IEEE International Conference on Multimedia & Expo Workshops (ICMEW)*, 2021. 2
- [26] Sara Fridovich-Keil, Giacomo Meanti, Frederik Rahbæk Warburg, Benjamin Recht, and Angjoo Kanazawa. K-planes: Explicit radiance fields in space, time, and appearance. In *Proceedings of the IEEE/CVF Conference on Computer Vision and Pattern Recognition*, pages 12479–12488, 2023. 2, 9
- [27] Quankai Gao, Qiangeng Xu, Hao Su, Ulrich Neumann, and Zexiang Xu. Strivec: Sparse tri-vector radiance fields. In

- Proceedings of the IEEE/CVF International Conference on Computer Vision*, pages 17569–17579, 2023. 2, 9
- [28] Vivek K. Goyal. Theoretical foundations of transform coding. *IEEE Signal Processing Magazine*, 18(5):9–21, 2001. 1
- [29] Zongyu Guo, Zhizheng Zhang, Runsen Feng, and Zhibo Chen. Causal contextual prediction for learned image compression. *IEEE Transactions on Circuits and Systems for Video Technology*, 2022. 2
- [30] Wang Guo-Hua, Jiahao Li, Bin Li, and Yan Lu. EVC: Towards real-time neural image compression with mask decay. In *The Eleventh International Conference on Learning Representations*, 2023. 1
- [31] Minghao Han, Shiyin Jiang, Shengxi Li, Xin Deng, Mai Xu, Ce Zhu, and Shuhang Gu. Causal context adjustment loss for learned image compression. In *Advances in Neural Information Processing Systems*, pages 133231–133253. Curran Associates, Inc., 2024. 1
- [32] D. He, Z. Yang, W. Peng, R. Ma, H. Qin, and Y. Wang. Elic: Efficient learned image compression with unevenly grouped space-channel contextual adaptive coding. In *2022 IEEE/CVF Conference on Computer Vision and Pattern Recognition (CVPR)*, 2022. 2, 7
- [33] Jia-Bin Huang, Abhishek Singh, and Narendra Ahuja. Single image super-resolution from transformed self-exemplars. In *Proceedings of the IEEE Conference on Computer Vision and Pattern Recognition (CVPR)*, pages 5197–5206, 2015. 6
- [34] Wei Jiang, Jiayu Yang, Yongqi Zhai, Peirong Ning, Feng Gao, and Ronggang Wang. Mlic: Multi-reference entropy model for learned image compression. In *Proceedings of the 31st ACM International Conference on Multimedia*, pages 7618–7627, 2023. 7
- [35] Joint Video Experts Team (JVET). VVCSoftware\_VTM - VTM-21.2. [https://vcgit.hhi.fraunhofer.de/jvet/VVCSoftware\\_VTM/-/tree/VTM-21.2](https://vcgit.hhi.fraunhofer.de/jvet/VVCSoftware_VTM/-/tree/VTM-21.2), 2023. Accessed: 2023-10-23. 1
- [36] J. Kim, J. Lee, and K. Lee. Accurate image super-resolution using very deep convolutional networks. In *2016 IEEE Conference on Computer Vision and Pattern Recognition (CVPR)*, pages 1646–1654, 2016. 2
- [37] Alexander Kirillov, Eric Mintun, Nikhila Ravi, Hanzi Mao, Chloe Rolland, Laura Gustafson, Tete Xiao, Spencer Whitehead, Alexander C. Berg, Wan-Yen Lo, Piotr Dollár, and Ross Girshick. Segment anything. *arXiv:2304.02643*, 2023. 6
- [38] A. Burakhan Koyuncu, Han Gao, Atanas Boev, Georgii Gaikov, Elena Alshina, and Eckehard Steinbach. Contextformer: A transformer with spatio-channel attention for context modeling in learned image compression. In *Proceedings of the European Conference on Computer Vision (ECCV)*, 2022. 2
- [39] A Burakhan Koyuncu, Panqi Jia, Atanas Boev, Elena Alshina, and Eckehard Steinbach. Efficient contextformer: Spatio-channel window attention for fast context modeling in learned image compression. *IEEE Transactions on Circuits and Systems for Video Technology*, 2024. 2, 5
- [40] C. Ledig, L. Theis, F. Huszar, J. Caballero, A. Cunningham, A. Acosta, A. Aitken, A. Tejani, J. Totz, Z. Wang, and W. Shi. Photo-realistic single image super-resolution using a generative adversarial network. In *2017 IEEE Conference on Computer Vision and Pattern Recognition (CVPR)*, 2017. 1, 2
- [41] Christian Ledig, Lucas Theis, Ferenc Huszár, Jose Caballero, Andrew Cunningham, Alejandro Acosta, Andrew Aitken, Alykhan Tejani, Johannes Totz, Zehan Wang, et al. Photo-realistic single image super-resolution using a generative adversarial network. In *Proceedings of the IEEE conference on computer vision and pattern recognition*, pages 4681–4690, 2017. 2
- [42] Jaewon Lee and Kyong Hwan Jin. Local texture estimator for implicit representation function. In *Proceedings of the IEEE/CVF conference on computer vision and pattern recognition*, pages 1929–1938, 2022. 3
- [43] A. Li, L. Zhang, Y. Liu, and C. Zhu. Feature modulation transformer: Cross-refinement of global representation via high-frequency prior for image super-resolution. In *2023 IEEE/CVF International Conference on Computer Vision (ICCV)*, 2023. 2
- [44] Daxin Li, Yuanchao Bai, Kai Wang, Junjun Jiang, Xianming Liu, and Wen Gao. Groupedmixer: An entropy model with group-wise token-mixers for learned image compression. *IEEE Transactions on Circuits and Systems for Video Technology*, 2024. 2, 5, 7
- [45] Han Li, Shaohui Li, Wenrui Dai, Maida Cao, Nuowen Kan, Chenglin Li, Junni Zou, and Hongkai Xiong. On disentangled training for nonlinear transform in learned image compression. In *The Thirteenth International Conference on Learning Representations*, 2025. 3
- [46] Wenbo Li, Xin Lu, Shengju Qian, Jiangbo Lu, Xiangyu Zhang, and Jiaya Jia. On efficient transformer-based image pre-training for low-level vision. *arXiv preprint arXiv:2112.10175*, 2021. 2
- [47] Xueting Li, Xiaolong Wang, Ming-Hsuan Yang, Alexei A Efros, and Sifei Liu. Scraping textures from natural images for synthesis and editing. In *European Conference on Computer Vision*, pages 391–408. Springer, 2022. 3
- [48] Jingyun Liang, Jiezhong Cao, Guolei Sun, Kai Zhang, Luc Van Gool, and Radu Timofte. Swinir: Image restoration using swin transformer. *arXiv preprint arXiv:2108.10257*, 2021. 2, 6, 7
- [49] Jingyun Liang, Yuchen Fan, Xiaoyu Xiang, Rakesh Ranjan, Eddy Ilg, Simon Green, Jiezhong Cao, Kai Zhang, Radu Timofte, and Luc V Gool. Recurrent video restoration transformer with guided deformable attention. *Advances in Neural Information Processing Systems*, 35:378–393, 2022. 10, 12
- [50] Jingyun Liang, Jiezhong Cao, Yuchen Fan, Kai Zhang, Rakesh Ranjan, Yawei Li, Radu Timofte, and Luc Van Gool. Vrt: A video restoration transformer. *IEEE Transactions on Image Processing*, 2024. 12
- [51] Bee Lim, Sanghyun Son, Heewon Kim, Seungjun Nah, and Kyoung Mu Lee. Enhanced deep residual networks for single image super-resolution. *2017 IEEE Conference on Computer Vision and Pattern Recognition Workshops (CVPRW)*, pages 1132–1140, 2017. 2

- [52] Bee Lim, Sanghyun Son, Heewon Kim, Seungjun Nah, and Kyoung Mu Lee. Enhanced deep residual networks for single image super-resolution. In *The IEEE Conference on Computer Vision and Pattern Recognition (CVPR) Workshops*, 2017. 1, 2, 6
- [53] Ce Liu and Deqing Sun. On bayesian adaptive video super resolution. *IEEE transactions on pattern analysis and machine intelligence*, 36(2):346–360, 2013. 10
- [54] Jie Liu, Wenjie Zhang, Yuting Tang, Jie Tang, and Gangshan Wu. Residual feature aggregation network for image super-resolution. In *Proceedings of the IEEE/CVF conference on computer vision and pattern recognition*, pages 2359–2368, 2020. 2
- [55] J. Liu, H. Sun, and J. Katto. Learned image compression with mixed transformer-cnn architectures. In *2023 IEEE/CVF Conference on Computer Vision and Pattern Recognition (CVPR)*. IEEE Computer Society, 2023. 1, 2, 5, 7, 8, 9, 10
- [56] Jinming Liu, Heming Sun, and Jiro Katto. Learned image compression with mixed transformer-cnn architectures. In *Proceedings of the IEEE/CVF Conference on Computer Vision and Pattern Recognition*, pages 14388–14397, 2023. 7
- [57] Sifei Liu, Shalini De Mello, and Jan Kautz. CosAE: Learnable fourier series for image restoration. In *The Thirty-eighth Annual Conference on Neural Information Processing Systems*, 2024. 2, 3
- [58] Ze Liu, Yutong Lin, Yue Cao, Han Hu, Yixuan Wei, Zheng Zhang, Stephen Lin, and Baining Guo. Swin transformer: Hierarchical vision transformer using shifted windows. In *Proceedings of the IEEE/CVF international conference on computer vision*, pages 10012–10022, 2021. 2
- [59] Ze Liu, Han Hu, Yutong Lin, Zhuliang Yao, Zhenda Xie, Yixuan Wei, Jia Ning, Yue Cao, Zheng Zhang, Li Dong, et al. Swin transformer v2: Scaling up capacity and resolution. In *Proceedings of the IEEE/CVF conference on computer vision and pattern recognition*, pages 12009–12019, 2022. 4, 10
- [60] I Loshchilov. Decoupled weight decay regularization. *arXiv preprint arXiv:1711.05101*, 2017. 7
- [61] Qi Mao, Tinghan Yang, Yinuo Zhang, Shuyin Pan, Meng Wang, Shiqi Wang, and Siwei Ma. Extreme image compression using fine-tuned vqgan models. 2023. 2
- [62] Qi Mao, Tinghan Yang, Yinuo Zhang, Shuyin Pan, Meng Wang, Shiqi Wang, and Siwei Ma. Extreme image compression using fine-tuned vqgan models. *ArXiv*, 2023. 2
- [63] D Martin, C Fowlkes, D Tal, et al. A database of human segmented natural images and its application to evaluating segmentation algorithms and measuring ecological statistics. In *Proceedings of the IEEE International Conference on Computer Vision (ICCV)*, pages 416–423, 2001. 6
- [64] Yusuke Matsui, Koichi Ito, Yuki Aramaki, et al. Sketch-based manga retrieval using manga109 dataset. *Multimedia Tools and Applications*, 76(20):21811–21838, 2017. 6
- [65] Ben Mildenhall, Pratul P Srinivasan, Matthew Tancik, Jonathan T Barron, Ravi Ramamoorthi, and Ren Ng. Nerf: Representing scenes as neural radiance fields for view synthesis. *Communications of the ACM*, 65(1):99–106, 2021. 4
- [66] David Minnen and Saurabh Singh. Channel-wise autoregressive entropy models for learned image compression. In *2020 IEEE International Conference on Image Processing (ICIP)*, pages 3339–3343, 2020. 7, 9
- [67] David Minnen, Johannes Ballé, and George D Toderici. Joint autoregressive and hierarchical priors for learned image compression. *Advances in neural information processing systems*, 31, 2018. 1
- [68] Thomas Müller, Alex Evans, Christoph Schied, and Alexander Keller. Instant neural graphics primitives with a multiresolution hash encoding. *ACM Trans. Graph.*, 41(4):102:1–102:15, 2022. 2, 4, 9
- [69] Seungjun Nah, Sungyong Baik, Seokil Hong, Gyeongsik Moon, Sanghyun Son, Radu Timofte, and Kyoung Mu Lee. Ntire 2019 challenge on video deblurring and super-resolution: Dataset and study. In *Proceedings of the IEEE/CVF conference on computer vision and pattern recognition workshops*, pages 0–0, 2019. 10
- [70] Maxime Oquab, Timothée Darcet, Theo Moutakanni, Huy V. Vo, Marc Szafraniec, Vasil Khalidov, Pierre Fernandez, Daniel Haziza, Francisco Massa, Alaaeldin El-Nouby, Russell Howes, Po-Yao Huang, Hu Xu, Vasu Sharma, Shang-Wen Li, Wojciech Galuba, Mike Rabbat, Mido Assran, Nicolas Ballas, Gabriel Synnaeve, Ishan Misra, Herve Jegou, Julien Mairal, Patrick Labatut, Armand Joulin, and Piotr Bojanowski. Dinov2: Learning robust visual features without supervision, 2023. 5, 10
- [71] Chenyang Qi, Xin Yang, Ka Leong Cheng, Ying-Cong Chen, and Qifeng Chen. Real-time 6k image rescaling with rate-distortion optimization. In *Proceedings of the IEEE/CVF Conference on Computer Vision and Pattern Recognition (CVPR)*, 2023. 7
- [72] Nasim Rahaman, Aristide Baratin, Devansh Arpit, Felix Draxler, Min Lin, Fred Hamprecht, Yoshua Bengio, and Aaron Courville. On the spectral bias of neural networks. In *International conference on machine learning*, pages 5301–5310. PMLR, 2019. 4
- [73] Oren Rippel and Lubomir Bourdev. Real-time adaptive image compression. In *Proceedings of the 34th International Conference on Machine Learning (PMLR)*, 2017. 2
- [74] Shuwei Shi, Jinjin Gu, Liangbin Xie, Xintao Wang, Yujiu Yang, and Chao Dong. Rethinking alignment in video super-resolution transformers. *Advances in Neural Information Processing Systems*, 35:36081–36093, 2022. 10, 12
- [75] Juan Song, Jiaxiang He, Mingtao Feng, Keyan Wang, Yunsong Li, and Ajmal Mian. High frequency matters: Uncertainty guided image compression with wavelet diffusion. *arXiv preprint arXiv:2407.12538*, 2024. 2, 5
- [76] Long Sun, Jinshan Pan, and Jinhui Tang. Shufflemixer: An efficient convnet for image super-resolution. In *Advances in Neural Information Processing Systems*, pages 17314–17326, 2022. 2
- [77] Ying Tai, Jian Yang, and Xiaoming Liu. Image super-resolution via deep recursive residual network. In *Proceedings of the IEEE conference on computer vision and pattern recognition*, pages 3147–3155, 2017. 2
- [78] Matthew Tancik, Pratul Srinivasan, Ben Mildenhall, Sara Fridovich-Keil, Nithin Raghavan, Utkarsh Singhal, Ravi Ra-

- mamoorthi, Jonathan Barron, and Ren Ng. Fourier features let networks learn high frequency functions in low dimensional domains. *Advances in neural information processing systems*, 33:7537–7547, 2020. 4
- [79] David Taubman and Michael Marcellin. *JPEG2000 Image Compression Fundamentals, Standards and Practice*. Springer Publishing Company, Incorporated, 2013. 1, 2
- [80] Joint Video Experts Team. Vvc official test model vtm. 2021. 7
- [81] Tong Tong, Gen Li, Xiejie Liu, and Qinquan Gao. Image super-resolution using dense skip connections. In *Proceedings of the IEEE international conference on computer vision*, pages 4799–4807, 2017. 2
- [82] G.K. Wallace. The jpeg still picture compression standard. *IEEE Transactions on Consumer Electronics*, 38(1):xviii–xxxiv, 1992. 1, 2, 6
- [83] Shen Wang, Zhengxue Cheng, Donghui Feng, Guo Lu, Li Song, and Wenjun Zhang. Asymllic: Asymmetric lightweight learned image compression. In *2024 IEEE International Conference on Visual Communications and Image Processing (VCIP)*, pages 1–5, 2024. 1
- [84] Xintao Wang, Ke Yu, Shixiang Wu, Jinjin Gu, Yihao Liu, Chao Dong, Yu Qiao, and Chen Change Loy. Esrgan: Enhanced super-resolution generative adversarial networks. In *Computer Vision – ECCV 2018 Workshops*, 2019. 2
- [85] Xintao Wang, Liangbin Xie, Chao Dong, and Ying Shan. Real-esrgan: Training real-world blind super-resolution with pure synthetic data. In *2021 IEEE/CVF International Conference on Computer Vision Workshops (ICCVW)*, 2021. 2
- [86] H. Wu, B. Xiao, N. Codella, M. Liu, X. Dai, L. Yuan, and L. Zhang. Cvt: Introducing convolutions to vision transformers. In *2021 IEEE/CVF International Conference on Computer Vision (ICCV)*, 2021. 2
- [87] Yueqi Xie, Ka Leong Cheng, and Qifeng Chen. Enhanced invertible encoding for learned image compression. In *Proceedings of the ACM International Conference on Multimedia*, pages 162–170, 2021. 7
- [88] Kai Xu, Ziwei Yu, Xin Wang, Michael Bi Mi, and Angela Yao. Enhancing video super-resolution via implicit resampling-based alignment. In *Proceedings of the IEEE/CVF Conference on Computer Vision and Pattern Recognition*, pages 2546–2555, 2024. 10, 12
- [89] Tianfan Xue, Baian Chen, Jiajun Wu, Donglai Wei, and William T Freeman. Video enhancement with task-oriented flow. *International Journal of Computer Vision*, 127:1106–1125, 2019. 10
- [90] R Zeyde, M Elad, and M Protter. On single image scale-up using sparse-representations. In *Proceedings of the International Conference on Curves and Surfaces (ICCS)*, pages 711–730, 2010. 6
- [91] Leheng Zhang, Yawei Li, Xingyu Zhou, Xiaorui Zhao, and Shuhang Gu. Transcending the limit of local window: Advanced super-resolution transformer with adaptive token dictionary. In *Proceedings of the IEEE/CVF Conference on Computer Vision and Pattern Recognition*, pages 2856–2865, 2024. 2, 4, 6, 10
- [92] Leheng Zhang, Yawei Li, Xingyu Zhou, Xiaorui Zhao, and Shuhang Gu. Transcending the limit of local window: Advanced super-resolution transformer with adaptive token dictionary. In *Proceedings of the IEEE/CVF Conference on Computer Vision and Pattern Recognition*, pages 2856–2865, 2024. 6, 7
- [93] Yulun Zhang, Kunpeng Li, Kai Li, Lichen Wang, Bineng Zhong, and Yun Fu. Image super-resolution using very deep residual channel attention networks. In *Proceedings of the European Conference on Computer Vision (ECCV)*, 2018. 2
- [94] Yulun Zhang, Yapeng Tian, Yu Kong, Bineng Zhong, and Yun Fu. Residual dense network for image super-resolution. In *Proceedings of the IEEE conference on computer vision and pattern recognition*, pages 2472–2481, 2018. 2
- [95] Shangchen Zhou, Jiawei Zhang, Wangmeng Zuo, and Chen Change Loy. Cross-scale internal graph neural network for image super-resolution. *Advances in neural information processing systems*, 33:3499–3509, 2020. 2
- [96] Qiang Zhu, Pengfei Li, and Qianhui Li. Attention retractable frequency fusion transformer for image super resolution. In *Proceedings of the IEEE/CVF Conference on Computer Vision and Pattern Recognition*, pages 1756–1763, 2023. 2
- [97] Yin hao Zhu, Yang Yang, and Taco Cohen. Transformer-based transform coding. In *International Conference on Learning Representations*, 2022. 2
- [98] Renjie Zou, Chunfeng Song, and Zhaoxiang Zhang. The devil is in the details: Window-based attention for image compression. In *CVPR*, 2022. 7